

# Multiphoton super-resolution imaging via virtual structured illumination

Sumin Lim<sup>1,2</sup>, Sungsam Kang<sup>1,2</sup>, Jin-Hee Hong<sup>1,2</sup>, Youngho Jin<sup>1</sup>, Kalpak Gupta<sup>1,2</sup>, Moonseok Kim<sup>3</sup>,  
Suhyun Kim<sup>4</sup>, Wonshik Choi<sup>1,2\*</sup>, Seokchan Yoon<sup>5\*</sup>

<sup>1</sup>*Center for Molecular Spectroscopy and Dynamics, Institute for Basic Science, Seoul 02841, Korea*

<sup>2</sup>*Department of Physics, Korea University, Seoul 02855, Korea*

<sup>3</sup>*Department of Medical Life Sciences, College of Medicine, The Catholic University of Korea, Seoul, 06591, Korea*

<sup>4</sup>*Department of Biomedical Sciences, Korea University, Ansan, Republic of Korea*

<sup>5</sup>*School of Biomedical Convergence Engineering, Pusan National University, Yangsan 50612, Korea*

\*Corresponding author(s). E-mail(s): [wonshik@korea.ac.kr](mailto:wonshik@korea.ac.kr); [sc.yoon@pusan.ac.kr](mailto:sc.yoon@pusan.ac.kr)

## Abstract

Fluorescence imaging in thick biological tissues is challenging due to sample-induced aberration and scattering, which leads to severe degradation of image quality and resolution. Fluorescence imaging in reflection geometry further exacerbates this issue since the point spread function is distorted in both excitation and emission pathways. Here, we propose a novel approach termed adaptive optics virtual structured illumination microscopy (AO V-SIM) that enables super-resolution multiphoton imaging through a scattering medium in reflection geometry. Our approach exploits the incoherent reflection matrix obtained using a conventional point-scanning fluorescence microscope with an array detector. We introduce V-SIM super-resolution reconstruction algorithm based on the incoherent reflection matrix. Furthermore, we introduce a software adaptive optics correction algorithm, AO V-SIM, which recovers unattenuated and phase-corrected optical transfer function for both excitation and emission pathways. The effectiveness of our proposed method is experimentally validated through sub-diffraction-limited two-photon fluorescence imaging of various samples in the presence of strong aberration.

## Introduction

Super-resolution fluorescence microscopy, which refers to imaging beyond the diffraction limit, is essential for advancing our understanding of biological science. Research over past years have resulted in several studies regarding various super-resolution methodologies. One of the most noteworthy example is structured illumination microscopy (SIM)<sup>1</sup>, which achieves super-resolution by illuminating the target with structured illuminations and subsequently synthesizing in the spatial frequency domain. Another methodology is image scanning microscopy (ISM)<sup>2</sup>, which uses pixel reassignment and shrinking of the PSFs in the final reconstruction process to achieve super-resolution. More advanced techniques-such as stimulated emission depletion microscopy (STED)<sup>3</sup>, which utilizes point-spread-function (PSF) engineering to obtain a tight focus below diffraction limit to illuminate the target, Stochastic optical reconstruction microscopy (STORM)<sup>4</sup> and photo-activated localization microscopy (PALM)<sup>5</sup>, which rely on the localization of individual fluorophore by stochastic activation or switching over time, and Super-resolution fluctuation imaging (SOFI)<sup>6</sup>, which performs temporal accumulation of fluorescence signals to achieve super-resolution have also been reported in the literature.

A common interest of any super-resolution imaging method is to achieve high signal-to-background ratio (SBR) and signal-to-noise ratio (SNR) at sub-micron scale resolution at depth deeper than 100 micrometers in biological

tissue specimens. However, when it comes to the practical implementation of these super-resolution techniques for deep tissue imaging, several challenges arise due to the presence of aberrations<sup>7</sup>. In the reflection geometry, both the emission and the excitation pathways are affected by aberrations. In conventional SIM methodologies, the excitation structured illumination is distorted due to tissue aberrations before it is incident on the desired object, and the emitted fluorescence signal is again distorted after excitation, which hinders the SIM reconstruction process and leads to loss of resolution, decrease in contrast, and generation of artifacts<sup>8</sup>. Similarly, two-photon fluorescence microscopy (2PFM), which is another mainstream deep tissue imaging technique, fails in the presence of severe aberrations.

A variety of hardware adaptive optics (AO) modalities have been developed to facilitate super-resolution by correcting wavefront errors in the presence of scattering and aberration. A common method is sensor-based AO<sup>9, 10</sup>, which employs a Shack-Hartmann wavefront sensor<sup>7</sup> or some other interferometric system to determine the wavefront errors. Wavefront shaping using deformable mirror (DM)<sup>7, 11</sup> or spatial light modulator (SLM)<sup>12</sup> is then performed to compensate for aberration and scattering during excitation of the target sample. Though direct and fast to implement, the primary disadvantages of sensor-based hardware AO lie in the requirement of highly complex optical setup and the relative lack of adjustability over different microscopy configurations<sup>13</sup>. Moreover, depending on the modality, additional measurement with nonlinear fluorescence guide stars may also be required for application of hardware AO correction on the emission pathway<sup>14</sup>. This can be either physically injected guide star or natural bright spot in the specimen. Simpler optical systems are required for sensor-less hardware AO methods, which involve optimization of the wavefront according to various image quality metrics like intensity and sharpness. These methods take long exposure time to find an optimized pattern for the DM or SLM, leading to photo damage as well as detrimental effects from vibrational noise. Often, even after hardware AO correction, the undesired detection of scattered photons due to residual aberration and scattering results in subpar optical sectioning performance as well as low-SNR and SBR in the AO corrected images<sup>15, 16</sup>. Additionally, multiphoton laser scanning microscopy combined with a DM to correct excitation pathway can have much longer penetration depth, but at the cost of resolution<sup>17</sup>.

To avoid the use of additional hardware components, software AO methods such as blind deconvolution and Richardson-Lucy deconvolution algorithms have been proposed. These models find a single emission intensity PSF and try to apply different types of blind deconvolution algorithms to a distorted image<sup>18</sup>. Since the excitation PSF is not considered in conventional deconvolution models, the image cannot be accurately recovered in the presence of strong aberration and scattering. Further, since these numerical methods are not physics-based without specific threshold limit of iteration process, they cannot differentiate signal and noise, and thus suffer from enhancement of noise or overcorrection of fine structures. In general, only either excitation or emission pathways are corrected in conventional AO methodologies. Most hardware or software AO methods don't correct both pathways due to the requirement of highly complex setups along with multiple rounds of measurements. However, correction of dual-pathway PSF distortions is essential to achieve super-resolution images from deep tissue specimen.

In this work, we propose a dual-pathway software AO correction method to achieve super-resolution in deep-tissue imaging. We first utilize a straightforward point-scanning setup to obtain a set of 2PF images and reconstruct it into an incoherent reflection matrix (IRM), which enables the application of an innovative super-resolution V-SIM methodology. Specifically, we reconstructed two-photon IRM and harnessed an aperture

synthesis reconstruction (SAR)<sup>19</sup>, similar to SAR performed in coherent imaging system<sup>20, 21</sup>. The SAR was applied in spatial frequency domain to the spectral IRM, which was obtained from Fourier transform of the IRM. The two-photon nonlinear incoherent imaging system is then analyzed in terms of optical transfer function (OTF) for both excitation and emission pathways<sup>22, 23</sup>. We developed an innovative software AO algorithm, denoted as the generalized deconvolution, which uses correlations between the acquired images to extract and correct modulation-phase retardations and attenuated amplitudes of the excitation and emission OTFs. Effectively, we employ a physics-based approach to iteratively solve the dual-pathway inverse problem<sup>22, 24</sup>. Notably, we independently correct input and output PSF distortions while simultaneously extending cut-off spatial frequencies of OTFs to obtain aberration-corrected spectral IRM, which leads to super-resolution image after aperture synthesis.

Applicability of our software AO algorithm in-situ to a simple multiphoton point-scanning setup facilitates a high versatility over various existing setup configurations. Exceptional optical sectioning is acquired by using two-photon excitation and aperture synthesis process, and our methodology itself can be widely combined to both coherent and incoherent light sources. Free from the post-measurement, we directly measure the fluorescence target specimen just once so that IRM is photo damage and vibration free with time efficiency. We successfully demonstrate our methodology through experiments on a wide variety of phantom and bio samples, such as USAF fluorescence resolution target, dyed beads, and mouse brain tissue samples. Our generalized deconvolution algorithm applied to the IRM yielded high SNR, high SBR, super-resolution, and high optical sectioning capabilities after application of our software AO to the recorded highly distorted and low-SNR fluorescence target specimen. We are able to achieve close to diffraction limit resolution, thus validating the universal applicability of our software AO algorithm. This plays a pivotal role in improving the identification of sub-micron-scale structures from different fluorescence target and bead specimen, without the requirement of any additional hardware AO devices.

## Results

### Virtual SIM by image scanning

V-SIM relies on measuring widefield intensity images of incoherent fluorescence emitted from a fluorescent object at various point-illumination positions. Let us consider sending a tightly focused excitation laser beam to the position  $\mathbf{r}_i$  in the plane of the fluorescent object through a heterogeneous scattering medium (Fig. 1a). The excitation laser beam undergoes deformation due to systematical and sample-induced aberration and scattering, characterized by the excitation intensity PSF, denoted  $h_{\text{ex}}(\mathbf{r})$ . The distorted laser beam interacts with a fluorescent target with fluorophore density distribution  $\gamma(\mathbf{r})$ . Emitted fluorescence from the target is once again subjected to aberration and scattering, this time characterized by the emission intensity PSF,  $h_{\text{em}}(\mathbf{r})$ . Then the fluorescence intensity at the detector plane  $\mathbf{r}_d$  with the point-illumination position  $\mathbf{r}_i$  can be described by the following equation:

$$f(\mathbf{r}_d; \mathbf{r}_i) = \int h_{\text{em}}(\mathbf{r}_d - \mathbf{r}) \gamma(\mathbf{r}) h_{\text{ex}}(\mathbf{r} - \mathbf{r}_i) d\mathbf{r}. \quad (1)$$

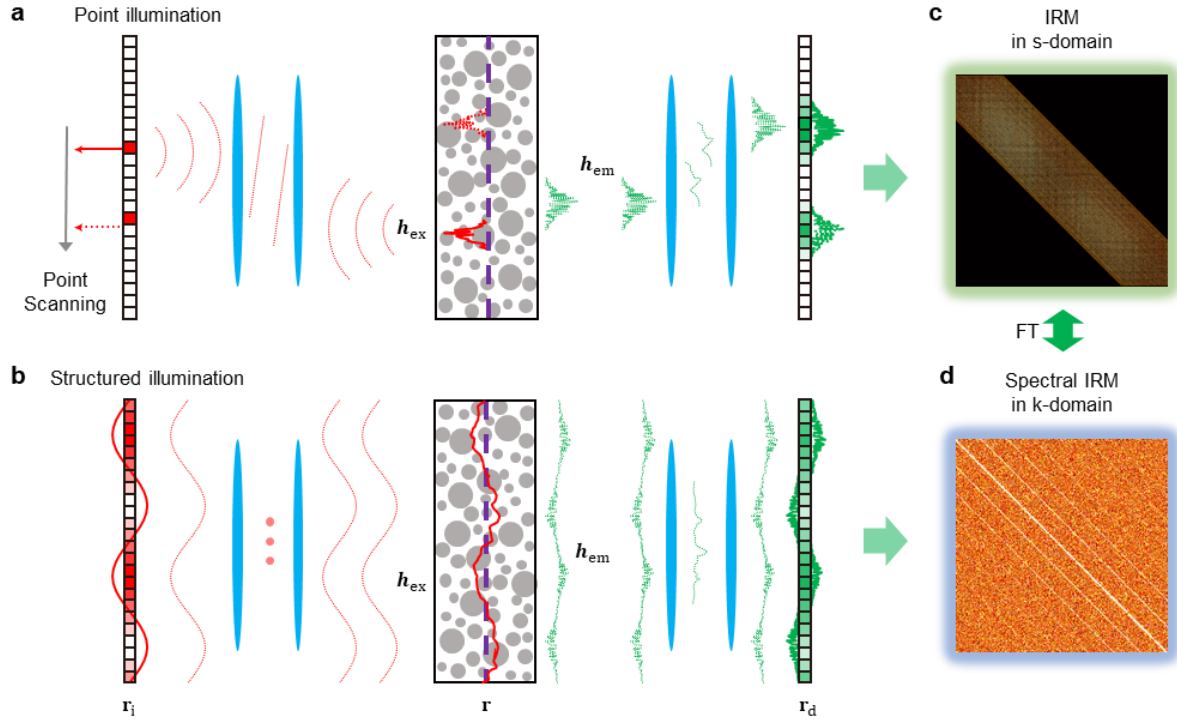


**Fig. 1 Schematic representation of virtual SIM methodology.** **a** A fluorophore target is embedded inside a scattering medium. Through point-scanning using coherent source, de-scanned convolved PSF images emitted from the fluorophore target are recorded with an array detector. The input illumination undergoes broadening twice due to sample-induced aberration and scattering in both the excitation and emission pathways, resulting in convolution of the input and output PSFs. **b** Equivalent in principle to (a), conventional raw SIM images can be obtained using Nyquist set of Moiré patterns. To obtain full-basis SIM images experimentally, an implementation of complete Nyquist set of incoherent periodic stripe patterns is required. **c** Convolved PSF images acquired in (a) are reconstructed into a fluorescence response matrix (FRM)  $f(\mathbf{r}_d; \mathbf{r}_i)$  in the spatial domain. **d** Raw SIM images obtained from process in (b) are reconstructed by finding a covariance matrix, spectral FRM  $F(\mathbf{k}_d; \mathbf{k}_i)$  in the spatial frequency domain. Alternatively,  $F$  can be also obtained by applying Fourier transform to  $f$ .

In the implementation, we scan the illumination position  $\mathbf{r}_i$  with a uniform scanning interval. For each illumination spot, a widefield fluorescence image is recorded with an array detector. The sampling interval is selected to satisfy the Nyquist sampling criterion for a desired spatial frequency bandwidth: For instance, the sampling interval can be set to one-quarter of an emission wavelength  $\lambda_{em}$  to achieve the maximum cut-off spatial frequency  $k_c$  for an imaging system with a numerical aperture of NA,  $k_c = 2(\text{NA})k_{em}$ , where  $k_{em} = 2\pi/\lambda_{em}$  is a wavenumber.

After acquiring a set of fluorescence images, we construct the incoherent IRM, denoted by  $f$ , whose element is given by  $f(\mathbf{r}_d; \mathbf{r}_i)$  (Fig. 1c). Essentially, this IRM contains the interrelation of both excitation and emission PSFs in the spatial domain. This description applies to multi-photon fluorescence imaging as well as one-photon fluorescence imaging as long as  $h_{em}$  is interpreted accordingly. In our study, we mainly considered two-photon fluorescence (2PF) imaging as it is better suited for deep-tissue imaging.

Once the incoherent IRM have been obtained, we can computationally synthesize the incoherent illumination to obtain fluorescence images for an arbitrary incoherent structured illumination pattern  $I_{st}(\mathbf{r}_i)$ :

$$f(\mathbf{r}_d; \mathbf{r}_i) = \int h_{em}(\mathbf{r}_d - \mathbf{r}) \gamma(\mathbf{r}) h_{ex}(\mathbf{r} - \mathbf{r}_i) I_{st}(\mathbf{r}_i) d\mathbf{r}. \quad (2)$$

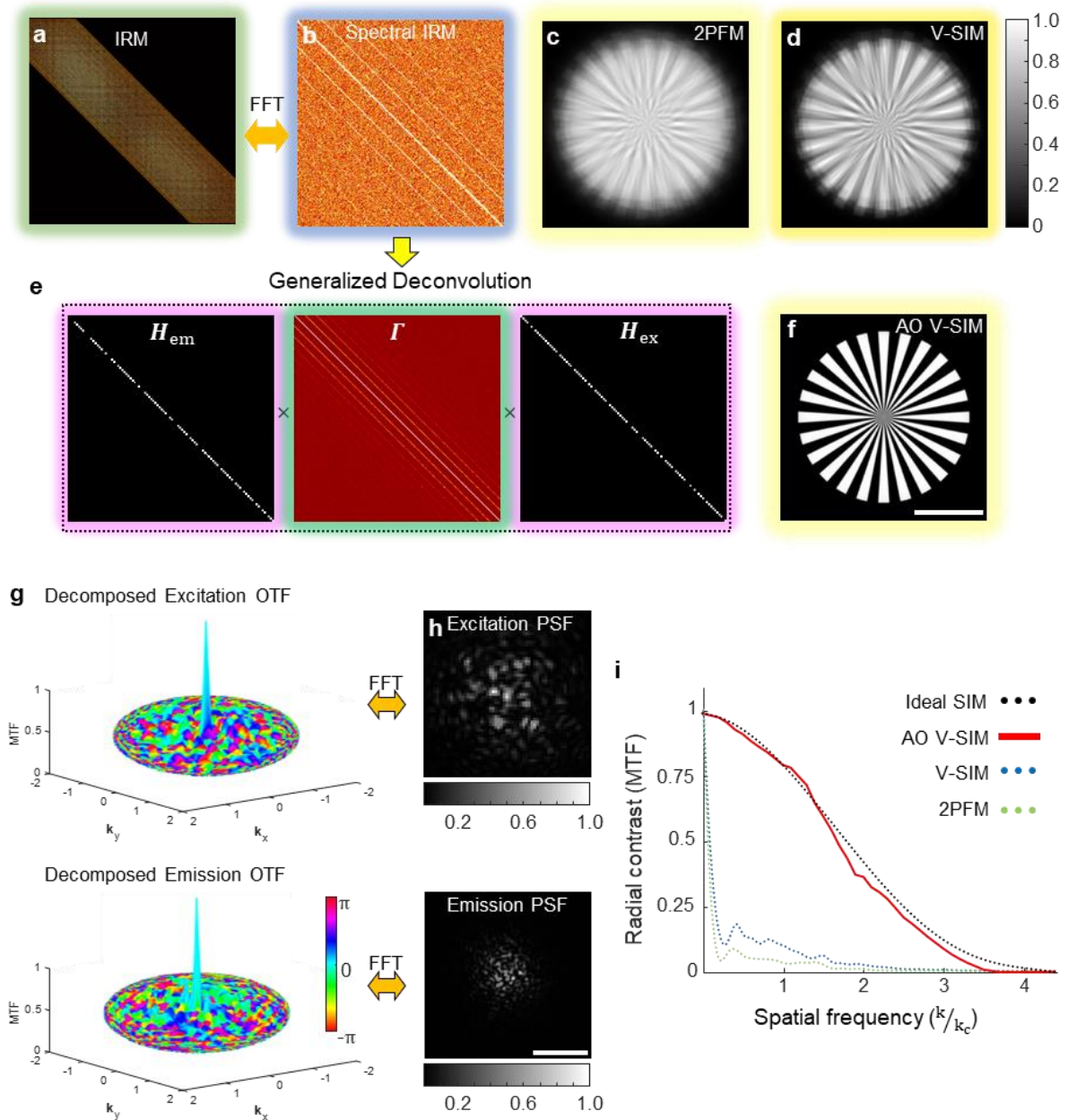


**Fig. 2** Aberration correction simulation using generalized deconvolution algorithm. **a** Simulated incoherent reflection matrix (IRM) in spatial domain for a Siemens Star fluorescent target. Excitation and emission PSFs are independently degraded by computationally generated artificial aberrations. **b** Spectral IRM in spatial frequency domain, obtained from Fourier transform of IRM. **c** 2PFM image reconstructed from IRM. **d** V-SIM image obtained by applying an aperture synthesis. **e** Generalized deconvolution of spectral IRM: decomposition of the spectral IRM into emission OTF ( $H_{em}$ ), power spectrum ( $\Gamma$ ), and excitation OTF ( $H_{ex}$ ). **f** AO V-SIM image obtained from the power spectrum matrix  $\Gamma$ . **g** Excitation and emission OTF maps. The height represents MTF, and color represents PTF. The spectral frequencies,  $k_x$  and  $k_y$  are normalized by  $k_c = 2(\text{NA})k_{em}$ . **h** Excitation and emission PSFs obtained by applying Fourier transform to the respective OTFs. **i** Radial averaged MTF obtained from the simulated images: 2PFM, ideal SIM, V-SIM, and AO V-SIM. Here, the ideal SIM image represents a V-SIM image obtained in the absence of aberrations.

For instance, a conventional SIM considers sending a 1D sinusoidal intensity pattern  $I_{st}(\mathbf{r}_i) = 1 + \cos(\mathbf{k}_i \cdot \mathbf{r}_i)$  with a modulation frequency  $\mathbf{k}_i$  and obtaining a spatial frequency spectrum of a fluorescence image  $F(\mathbf{k}_d; \mathbf{k}_i)$ . We can obtain equivalent information by applying a virtual structured illumination  $I_{st}(\mathbf{r}_i) = e^{i\mathbf{k}_i \cdot \mathbf{r}_i}$  to IRM in Eq. (2) and taking Fourier transform of  $f(\mathbf{r}_d; \mathbf{r}_i)$ :

$$F(\mathbf{k}_d; \mathbf{k}_i) = H_{em}(\mathbf{k}_d) \Gamma(\mathbf{k}_d - \mathbf{k}_i) H_{ex}(\mathbf{k}_i). \quad (3)$$

This process is illustrated in Fig. 1b, where we can extract the spatial frequency response of fluorescence emission from the synthesis. Here  $H_{ex}$ ,  $\Gamma$ , and  $H_{em}$  are Fourier transform of  $h_{ex}$ ,  $\gamma$ , and  $h_{em}$ , respectively.  $H_{ex}$  and  $H_{em}$  correspond to the optical transfer functions (OTFs) of excitation and emissions. Figure 1d shows the spectral incoherent reflection matrix  $\mathbf{F}$  whose element is given by  $F(\mathbf{k}_d; \mathbf{k}_i)$ . In case there is no aberration and scattering, each column of  $\mathbf{F}$  corresponds to  $\Gamma(\mathbf{k}_d - \mathbf{k}_i)$  with the bandwidth set by  $|\mathbf{k}_d - \mathbf{k}_i| \leq k_c$ , and the Fourier weighting set by  $H_{em}(\mathbf{k}_d)$ . By aperture synthesis process,  $\sum_{\mathbf{k}_i} F(\Delta\mathbf{k} + \mathbf{k}_i; \mathbf{k}_i)$ , we can expand the spectral bandwidth by a factor of two, which leads to the super-resolution image reconstruction. Essentially, this is the image reconstruction principle of conventional structured illumination microscopy (SIM).

#### Retrieval of excitation and emission OTFs from incoherent RM

In fluorescence imaging, excitation and emission pathways are independently affected by sample-induced aberration and scattering due to their different wavelengths. To correct for these aberration and scattering, we need to obtain their complex-valued OTFs,  $H_{em}$  and  $H_{ex}$ . Equation (3) can be written as the following matrix multiplication form:

$$\mathbf{F} = \mathbf{H}_{em} \mathbf{\Gamma} \mathbf{H}_{ex}, \quad (4)$$

where  $\mathbf{\Gamma}$  is a Toeplitz matrix representing the power spectrum matrix of the fluorescent target, and  $\mathbf{H}_{em}$  and  $\mathbf{H}_{ex}$  are two diagonalized matrices representing the excitation and emission OTFs, respectively. We developed a generalized matrix decomposition algorithm to separately identify  $\mathbf{H}_{em}$ ,  $\mathbf{\Gamma}$ , and  $\mathbf{H}_{ex}$  from  $\mathbf{F}$  by solving the dual inverse problem. The key concept is to obtain the approximate excitation and emission OTFs by sequentially estimating the correlations among columns and rows of the spectral FRM, respectively. Since OTFs are decreased in magnitude at high spatial frequencies, it is important to properly normalize their magnitude to achieve full-bandwidth resolution. To this end, we developed an estimate of complex Wiener filters from excitation and emission OTFs, respectively. Two empirically set regularization factors were used to calculate the excitation and emission complex Wiener filters from the obtained OTFs. These regularization factors are essentially noise-to-signal ratios, determining the level of noise threshold for suppressing noise while solving the dual-inverse problem. Finally, we multiplied the obtained complex Wiener filters by the spectral IRM. By repeating this process iteratively, our algorithm gradually finds the OTFs. Notably, conventional blind-deconvolution ignores  $h_{ex}$  and finds a single PSF at the emission pathway, which is approximated as  $h_{em}$ . However, this assumption is valid only for wide-field illumination. In the case of point-scanning fluorescence or structured illumination, finding  $h_{ex}$  is critical for achieving super-resolution imaging, which is a unique aspect of the presented method compared to conventional blind deconvolution applied.

To validate our algorithm, we conducted an algorithm performance analysis with a simulated IRM data according to our proposed point-scanning geometry (Fig. 1a). This simulated data employed an emission wavelength of  $\lambda_{em} = 520$  nm and a NA of 1. For simplicity, we assume that the excitation wavelength is roughly twice of the emission wavelength, i.e.,  $\lambda_{ex} \approx 2\lambda_{em}$ , so that the cut-off spatial frequencies for excitation and emission OTFs are the same. Therefore, a theoretically achievable resolution is a quarter of the fluorescence wavelength,  $\lambda_{em}/4 = 130$  nm. To introduce wavefront distortion, we computationally added aberrations to both excitation and emission PSFs. The two PSFs were generated by adding random superposition of Zernike modes in the excitation and emission pupil planes. Typically, we added Zernike modes up to the order of 30 with various mode coefficients. To simulate two-photon excitation, we took the square of the absolute square of the Fourier transform of the complex pupil function for the two-photon excitation PSF. The emission PSF was obtained by the absolute square of the Fourier transform of the complex pupil function. We simulated the point-scanning data acquisition process by multiplying excitation PSF with the target in the spatial domain and subsequently convolving emission PSF in the spatial domain. Figure 2a visualizes the constructed IRM from this point-scanning simulation. We constructed an image equivalent to conventional (2PFM) imaging by integrating all pixel values column-wise from the IRM (Fig. 2c). We obtained spectral IRM, converting the basis of IRM to spatial frequency by taking Fourier transform of IRM along both column and row (Fig. 2b). We then obtained a V-SIM image from the spectral IRM using aperture synthesis (Fig. 2d). The V-SIM image was blurred due to the presence of aberrations and scattering.

Next, we applied our matrix decomposition algorithm to the spectral IRM to validate the aberration correction performance of AO V-SIM. This involved the decomposition of the spectral IRM in Fig. 2b into three distinct matrices (Fig. 2e): Excitation and emission OTF matrices,  $\mathbf{H}_{em}$  and  $\mathbf{H}_{ex}$ , and a target power spectrum matrix,  $\mathbf{I}$ . These OTF matrices obtained from decomposition are visualized in Fig. 2g. Here, the amplitude and phase of the OTF, which are respectively termed modulation transfer function (MTF) and phase transfer function (PTF), are visualized by height and color, respectively. The widths of MTFs were substantially reduced with complex phase distribution in PTF due to aberration in this case. We obtained the excitation and emission PSF images by applying the Fourier transform to the respective OTF maps (Fig. 2h). The PSFs were specular due to the aberration.

We obtained the AO V-SIM image (Fig. 2f) from the aperture synthesis of the columns of the  $\mathbf{I}$  identified by the matrix decomposition. The originally blurred image was made sharper with a resolution close to  $\lambda_{em}/4$ . The reconstructed image has a correlation of 0.98 with respect to the V-SIM image without aberration. We quantified the aberration correction power of our algorithm by calculating the MTF of the reconstructed Siemens-star microscopies in Fig. 2. Specifically, we determined the MTF values for each spatial frequency by extracting circular intensity profiles for each radius and measuring contrast values from the profile. The red curve in Fig. 2i shows the obtained MTF of the AO V-SIM image in Fig. 2f. This was almost identical to the ideal MTF obtained for the SIM image without aberration (black dotted curve). The MTFs obtained from two-photon image (Fig. 2c) and V-SIM without aberration correction (Fig. 2d) are displayed as dotted blue and green curves, respectively. These MTFs present substantial loss of information at high spatial frequencies.

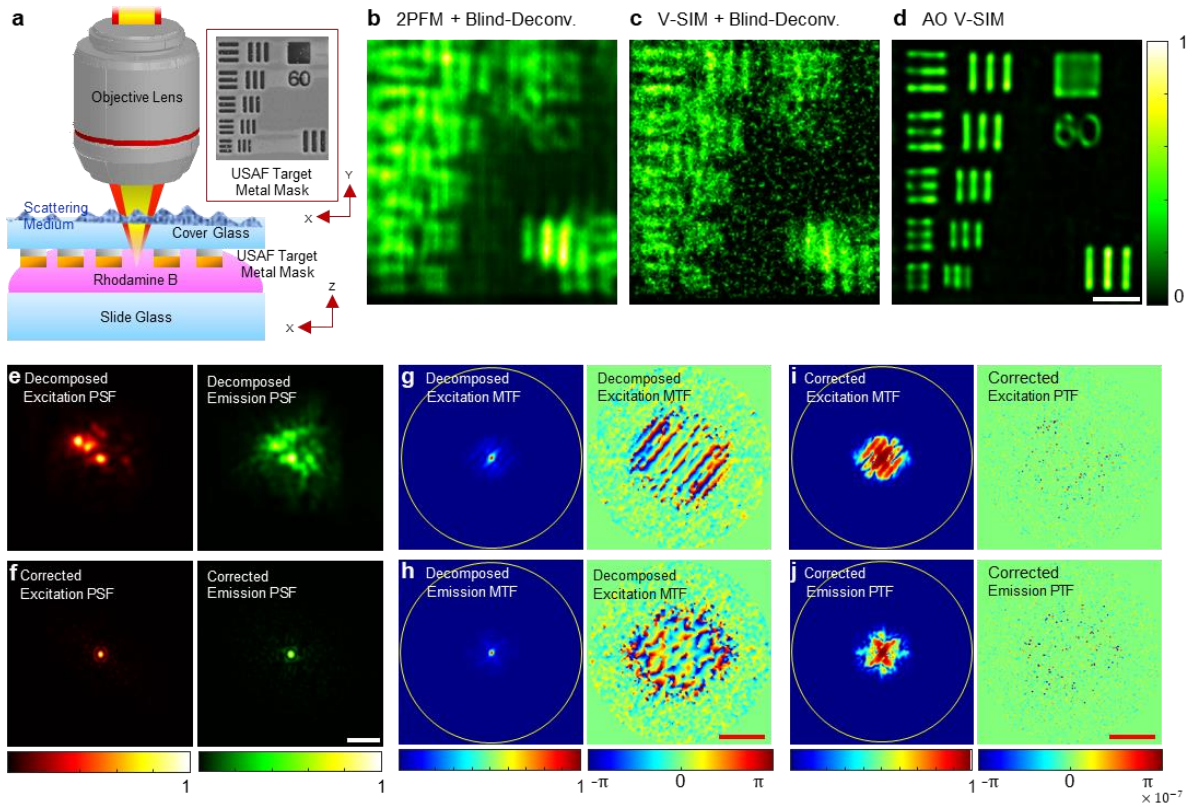


**Fig. 3 Demonstration of the super-resolution imaging a fluorescent resolution target through a scattering medium with severe aberrations and scattering.** **a**, Illustration of imaging geometry. Inset: An in-house fabricated fluorescence resolution target with sub-micron-scale patterns. **b**, 2PFM image. **c**, V-SIM image. **d**, AO V-SIM image. **e**, Excitation (left) and emission (right) PSF images before AO correction. **f**, Excitation (left) and emission (right) effective PSFs after AO correction. **g**, Decomposed excitation OTF maps before AO correction: here, MTF map (left) and PTF map (right) are shown. **h**, Same as **g**, but for emission OTF. **i-j**, Identical to **g-h**, but for effective OTF maps after AO correction. All images in **b-d** are normalized to a range of 0 to 1. The PSF and MTF maps in **e-j** are normalized to a range of 0 to 1. Scale bars in **b-d**, 2  $\mu\text{m}$ . Scale bar in **e-f**, 2.5  $\mu\text{m}$ .

### Experimental validation of super-resolution multi-photon AO V-SIM

We experimentally validated the performance of the proposed computational AO super-resolution multi-photon microscopy by imaging a fluorescent target under severe aberration conditions. The fluorescent target was fabricated by placing a thin metal mask of an etched USAF target pattern onto a Rhodamine B solution. An artificially-made scattering medium was superimposed on top of the metal mask to introduce aberration and scattering (see fluorescence target fabrication in Methods). We acquired two-photon fluorescence images of the fluorophore target using the point-scanning via widefield-detection method, as illustrated in Fig. 3a (see also Experimental setup in Method). After obtaining two-photon images of a complete basis set for illumination points, we constructed an IRM and proceeded with the image reconstruction according to the previously discussed microscopy modalities: 2PFM (Fig. 3b), V-SIM (Fig. 3c), and AO V-SIM (Fig. 3d).

The AO V-SIM image shows a clear, high-contrast structure, whereas the 2PFM and V-SIM images are severely blurred with multiple ghost artifacts due to strong aberrations. The smallest line spacings in the resolution target, which are 310 nm measured with SEM, were well resolved in the AO V-SIM image. Furthermore, SBR and SNR,



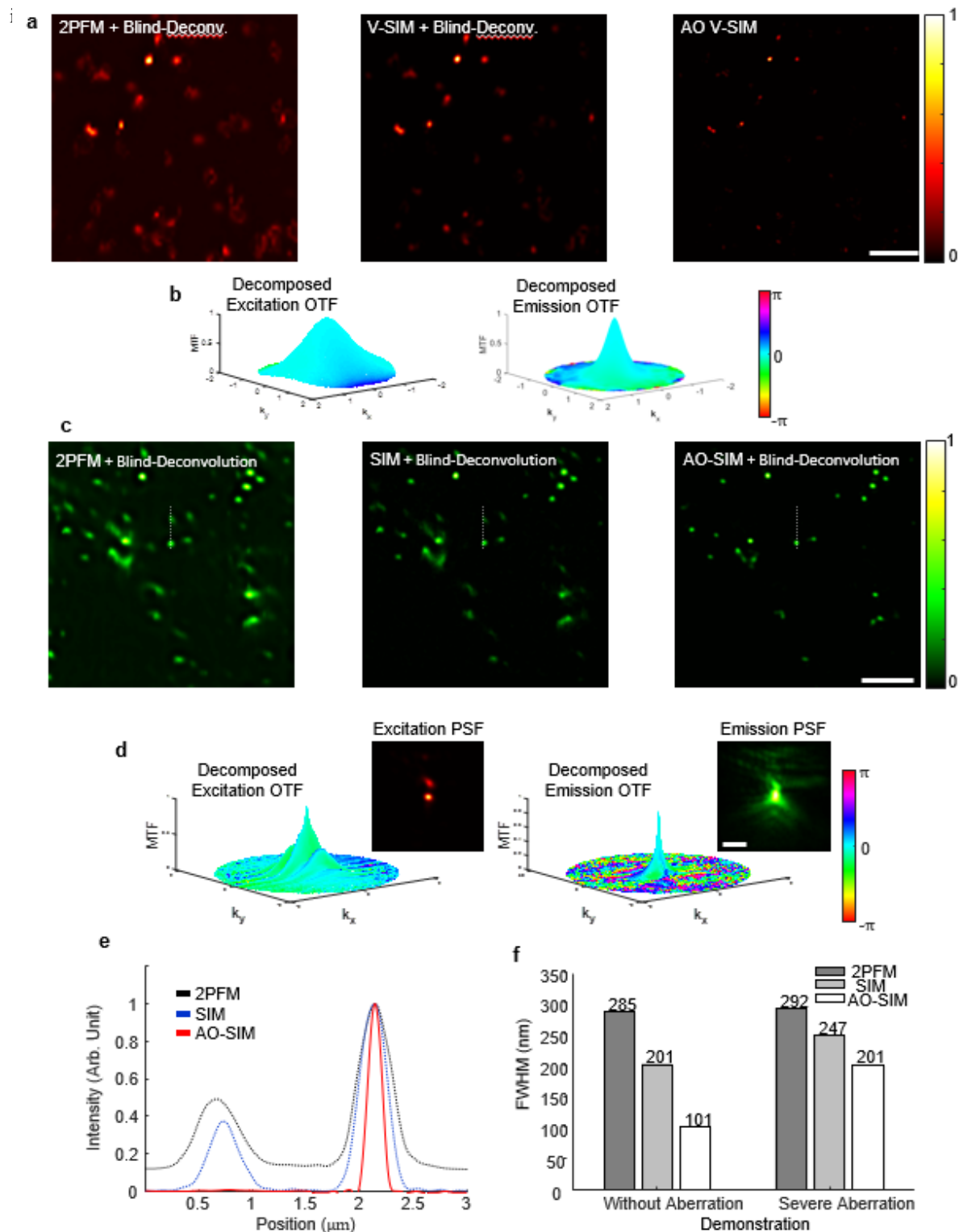


**Fig. 4 Validation of super-resolution using bead particles.** **a** 2PFM (left), V-SIM (center), and AO V-SIM images for 100-nm-diameter Rhodamine B polystyrene beads without aberration. **b** Excitation OTF (left) and emission OTF map (right) decomposed by the generalized deconvolution algorithm. Here, height represents MTF and color represents PTF. **c** Images for 100-nm-diameter Alexa 488 stained gold particles with an artificial aberrating medium. **d** Excitation OTF (left) and emission OTF map (right). Both excitation and emission MTFs are substantially attenuated compared to **(b)** due to strong aberrations. **e** Line profiles along white dotted lines in **(c)**. A peak shown at a position around 0.5 to 1  $\mu\text{m}$  in 2PFM (black) and SIM (blue) profiles is ghost artifacts. **f** FWHMs of the brightest particles in **(a, c)**. Scale bars in **(a, c)**, 2  $\mu\text{m}$ .

Quantitative analysis determined the SBR factors in the case of 2PFM, V-SIM, and AO V-SIM to be 6.3, 17.4 and 147.2, respectively.

AO V-SIM also offers the unique capability of decomposing the excitation and emission OTFs through the generalized deconvolution algorithm. The decomposed excitation and emission OTF maps before AO correction are shown in Fig. 3g and 3h, respectively. The corresponding decomposed PSFs (Fig. 3e) exhibit multiple foci, indicating strong wavefront distortions arising from the scattering medium. These multi-focal PSFs are responsible for the ghost artifacts in the images. Our algorithm retrieves both PTFs and MTFs over high spatial frequency components and computationally corrects aberration by multiplying both the decomposed excitation and emission OTFs by complex Wiener filters. The corrected OTFs after the aberration correction (Figs. 3i and j) show that the PTF distortions are almost resolved, and the widths of MTFs are substantially broadened. As a result, the decomposed PSFs are converted into a single, sharp, Gaussian-like PSF (Fig. 3f). This generalized deconvolution algorithm, capable of finding excitation and emission OTFs, enables more accurate image reconstruction compared to conventional blind deconvolution relying solely on an emission PSF, especially in the presence of strong aberrations.

For validation of the super-resolution imaging capability, we conducted two sets of experiments, one using Rhodamine B polystyrene beads without a scattering medium and the other with Alexa 488 stained gold particles with a scattering medium. Their peak emission wavelengths are respectively 567 nm and 520 nm. The diameter of both the beads and particles was 100 nm. 2PFM, V-SIM, and AO-SIM images acquired from the Rhodamine B beads obtained in the absence of scattering medium are shown in Fig. 4a (see experimental configuration in Methods). The SAR process incorporated into the V-SIM image resulted in significantly better optical-sectioning performance compared to the 2PFM image with substantial resolution enhancement. We then applied our algorithm to the IRM and obtained excitation and emission OTFs (Fig. 4b). PTFs were mostly flat due to the absence of aberration. However, there were decreases in MTFs at high spatial frequencies. This is pronounced in the emission OTF because it is more affected by system aberration due to shorter wavelengths and leads to smaller effective OTF. Since our algorithm corrects both the PTFs and MTFs, we can exploit the full bandwidth of OTFs, achieving a resolution close to the theoretical limit. We measured the spatial resolution for each imaging modality (Fig. 4f, without aberration). FWHM values measured from Rhodamine B beads in 2PFM, V-SIM, and AO-SIM images were 306 nm, 225 nm, and 164 nm, respectively, obtained by averaging the horizontal and vertical FWHM values from 5 brightest beads. Notably, these measured FWHM values of 2PFM, V-SIM, and AO-SIM images were approximately equal to their expected values for each imaging modality. Thus, after the application of our generalized deconvolution algorithm, we obtained a lateral resolution close to an ideal super-resolution.

Following the same imaging step as before, we constructed the 2PFM, V-SIM, and AO-SIM images of the Alexa 488 stained gold particles with a severe scattering medium (Fig. 4c). Excitation and emission OTF maps obtained by our algorithm are presented in Fig. 4d. These superimposed OTF maps comprise the experimental correction for both systematical OTFs and the scattering medium-induced OTFs. Both excitation and emission MTF maps in Fig. 4d fall sharply from the center compared to those shown in Fig. 4b, thus extensively reducing the effective MTF bandwidths. We extracted intensity profiles from white dotted lines in Fig. 4c. These intensity profiles of 2PFM and V-SIM are represented in Fig. 4e by black and blue dotted lines and show ghost artifacts within the position range from 0.5 to 1 micrometer. This is because the MTF is modulated along the  $k_y$  direction,

which leads to the split foci PSF. However, our algorithm could completely correct this artifact and recover a single sharp PSF, as evidenced by the line profile obtained from the AO V-SIM image (indicated in red). Similar to the previous case, we measured spatial resolution for each imaging modality (Fig. 4f, with severe aberration) from the 5 brightest particles. Identical to previous measurement, FWHM values were measured from the single Gaussian peaks at actual particle positions within three imaging modalities. The FWHM values measured in 2PFM, V-SIM, and AO V-SIM images were 439 nm, 367 nm, and 289 nm, respectively. AO V-SIM image showed the sharpest resolution compared to other imaging modalities, in addition to removing the ghost artifacts present in 2PFM and V-SIM images. However, the achieved resolution is about twice as large as the theoretical limit.

### **Mouse Brain Imaging**

In our endeavor of enhancing the practical utility of our imaging techniques, we transitioned our experimental focus to imaging a Thy1-EGFP immunolabeled ex-vivo mouse brain. Utilizing two-photon eGFP fluorescence, we imaged dendritic spines of neurons expressing GFP at various depths within a 500- $\mu\text{m}$ -thick section of the mouse brain cortex, specifically through a coronal section.

Figures 5a-c show the 2PFM, V-SIM, and AO V-SIM images reconstructed from a depth of 130  $\mu\text{m}$ . Magnified views of the regions marked by white dotted boxes are presented as insets in their respective images. 2PFM image in Fig. 5a shows somewhat blurred dendritic structures. In contrast, the V-SIM image in Fig. 5b reveals a markedly clearer depiction of dendrites and dendritic spines<sup>12</sup>. However, the shapes of some of the dendritic spines and their neck thicknesses are not distinctly visible, and SNR is low. On the contrary, our algorithm could provide super-resolution images of these dendritic spines and their necks with enhanced resolution and SNR. Notably, the AO V-SIM image consistently provides the thinnest measured dendritic spine necks, approaching the theoretical super-resolution limit of SIM.

Figures 5f-h show 2PFM, V-SIM, and AO V-SIM images reconstructed at an imaging depth of 180  $\mu\text{m}$ . Magnified views of the regions marked by white dotted boxes are presented as insets in their respective images. 2PFM image in Fig. 5f shows somewhat blurred dendritic structures. Employing our methodology, it was seen that the V-SIM image in Fig. 5g reveals a clear depiction of dendrites and dendritic spines<sup>12</sup>. However, the shapes of some of the dendritic spines and their neck thicknesses are not distinctly visible. The AO V-SIM (Fig. 5h) provides a markedly clearer image with an enhanced resolution and SNR.

### **Discussion**

We successfully implemented a versatile AO V-SIM imaging technique to achieve well-corrected super-resolution images even in the presence of severe aberration and scattering. A point-scanning setup identical to that of ISM was deployed for accurate AO correction and high depth-sectioning inside the scattering medium, supporting augmentation over both conventional SIM and ISM modalities. To correct the distorted PSF at each position within the fluorescence target, we measured a complete set of images within the Nyquist limit of intensity

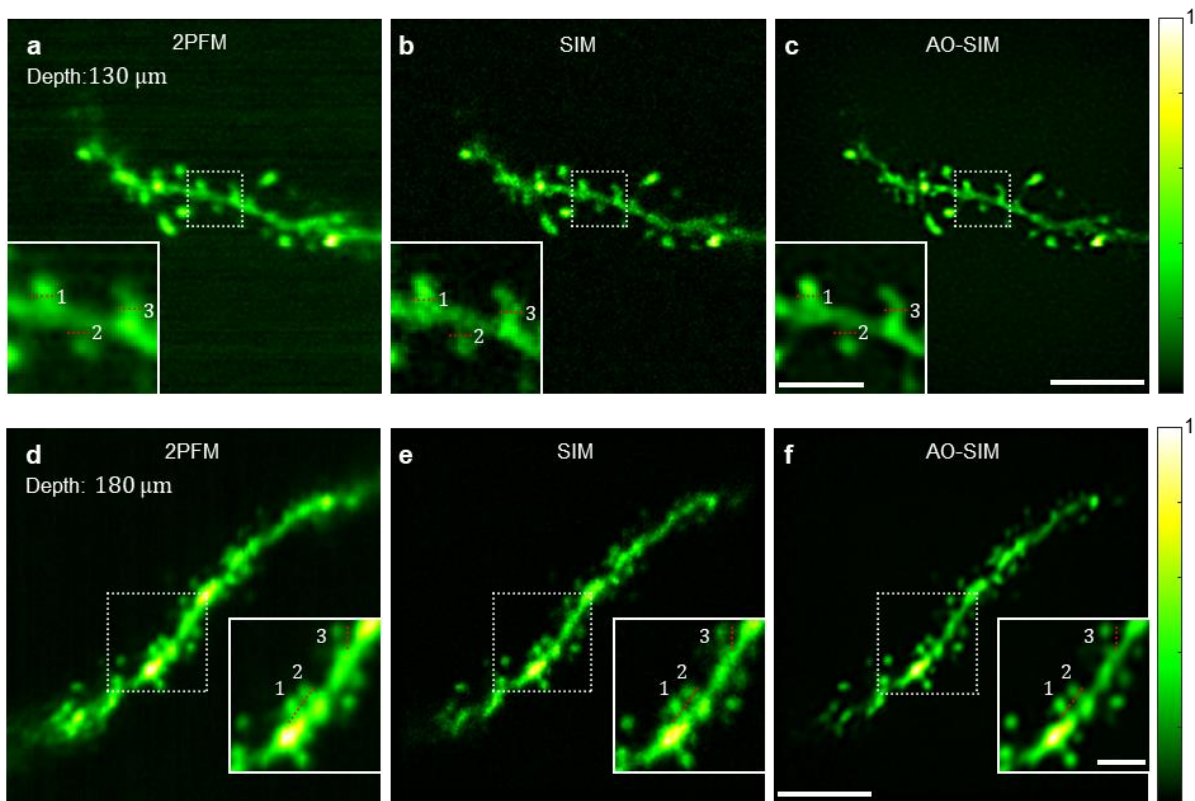


**Fig. 5 Mouse brain imaging.** a-c Thy1-EGFP immunolabeled ex-vivo mouse brain was imaged with our microscopy technique at a depth of 130  $\mu\text{m}$ . 2PFM (a), SIM (b), and AO-SIM (c) images are reconstructed. Magnified views of regions indicated by white dotted boxes in (a-c) are shown in inset. d-f, Same as (a-e), for a deeper depth of 180  $\mu\text{m}$ . It is discernible that the AO-SIM images have substantially better resolution and SNR after application of software AO correction for both depths. Here, (a-f) have been normalized according to a scale ranging from 0 to 1. Scale bar in the dendrite images (a-f), 5  $\mu\text{m}$ . Scale bar in insets of (a-f), 2  $\mu\text{m}$ .

basis. We collected these highly distorted PSF and reconstructed them to approximately the super-resolution limited PSFs. The application of our generalized deconvolution algorithm to the acquired data resulted in enhancement to the quality of super-resolution images without the need for nonlinear fluorescence guide star or any additional hardware AO devices, as well as without any prior knowledge about the fluorophore target. Thus, this process enabled the recovery of the OTFs associated with the excitation and emission processes by calculating complex Wiener filters in the spatial frequency domain, resulting in the attainment of the super-resolution fluorescence power spectrum in reflection mode. Subsequently, the application of aperture synthesis led to super-resolution AO V-SIM image while effectively suppressing noise.

The methodology was verified through both simulations and experiments on a variety of samples. First, the feasibility of the method was established numerically (Fig. 2). Our generalized deconvolution algorithm notably rectified the ghost artifacts, showing outstanding AO performance even in the presence of highly-scattering medium (Fig. 3). Further verification of the super-resolution capability and AO performance of our method was once more performed using 100 nm diameter fluorescent-dyed beads and gold particles (Fig. 4). The potential of AO V-SIM for image resolution enhancement at depths greater than 100  $\mu\text{m}$  inside the mouse brain tissue (Fig. 5) and zebrafish hindbrain (see Extended Fig. 3) was demonstrated.

Our decomposition method surpasses the capabilities of conventional single blind-deconvolution models based on intensity profile analysis. This is corroborated by our experiment using USAF resolution fluorescence target in the presence of severe aberrations. Since we obtain the excitation and emission OTFs using correlations from the full measured matrix, our approach inherently provides an accurate aberration-corrected target in comparison to that obtained using the conventional blind-deconvolution algorithms combined with hardware AO devices. Moreover, our iterative OTF inverse solver accompanied with two independent regularizations in dual-pathways provided an authentic method for estimating highly-accurate distorted PSFs. Further, we clarified that our methodology framework persistently remains valid for multiphoton fluorescence imaging in typical cells and standard animal tissue studies, even comparable to hardware AO corrected SIM images, depending on the severity of the scattering<sup>15</sup>.

However, there do exist limitations to our methodology. The fluorescence signal may be obscured below the noise level due to lack of excitation laser power and depth-dependent background scattering. This would lead to a rapid decline in the high spatial frequency components of MTFs, making the PSF retrieval process challenging due to lack of signal. In such cases, hardware AO correction would have to be implemented in order to raise the signal above a certain SNR threshold by correcting excitation pathway in advance, before our algorithm can be used to maximize OTF bandwidth.

In conclusion, our work presented the efficacy of AO V-SIM within a simplified point-scanning configuration without using any hardware correction. We anticipate the prompt integration of our technique into commercial multiphoton microscopic systems. Future strategies include the use of AO V-SIM to enable in-vivo imaging. This will necessitate additional implementation of methods such as parallel imaging using multifocal PSFs<sup>25, 26</sup>, utilizing a DMD or SLM in PSF engineering<sup>27-31</sup>. Similarly, employing an advanced detector like a SPAD array detector<sup>32</sup> or an EMCCD array detector<sup>33</sup> may also prove beneficial in capturing high-SNR signals. Progressively, these efforts are aimed at accelerating total image acquisition speed and improving the image quality of raw PSF data with superior detector sensitivity performance beyond current levels.

## **Methods**

### **Fluorescence target fabrication**

First, we deposited 40-nm-thick titanium and 40-nm-thick gold layers on a cover glass with a thickness of 500  $\mu\text{m}$ . The titanium metal serves as an adhesion layer between gold and glass, and both gold and titanium metal act as a metal mask, meeting the necessary conditions to remain unaffected by skin-depth. Next, we created a customized USAF resolution target pattern using the FIB etcher. Through an etching process that removed the entire gold and titanium, the residual metal on the target pattern formed a mask to conceal background fluorescence. Following this, we prepared a solution of Rhodamine B (MFCD00011931, Sigma-Aldrich) in ethanol, diluted to one-hundredth of the maximum solubility of Rhodamine B in ethanol. The fluorescence solution was then poured into a well created by a double-sided sticker spacer (654002, Grace Bio-Labs). The fabricated target mask was flipped over and stuck on the spacer. Finally, an artificially-made scattering medium with a cleaning polymer solution (FCDFR, First Contact) was attached to the surface of a 130- $\mu\text{m}$ -thick cover glass. The surface of the cleaning polymer was intentionally roughened by scratching it with a sandpaper.

### **Experimental configuration**

We have established a straightforward two-photon point-scanning microscope configuration customized for our research objectives. In our setup, a femtosecond pulsed laser (INSIGHT X3, Spectra Physics) with a central wavelength of 900 nm was utilized as the excitation source for Alexa 488 and eGFP fluorescence, and 850 nm was used for Rhodamine B. A short-pass dichroic mirror (DMSP680B, Thorlabs) was used to separate the emitted fluorescence from the excitation laser beam. The excitation laser beam underwent raster-scanning through 2D Galvano mirrors (GVS002, Thorlabs) before being focused onto the target via a high-numerical-aperture objective (N60X-NIR, Nikon,  $\times 60$ , 1.0 NA). Given that the fluorophores emitted green fluorescence signals of 530 nm (Alexa 488, GFP, and eGFP) and yellow fluorescence signals of 565 nm (Rhodamine B), these signals were de-scanned by the 2D Galvano mirrors. Subsequently, they traversed through the previous short-pass dichroic mirror, a short-pass filter (FESH0700, Thorlabs), and a band-pass filter (selectively employed according to the type of fluorescent dye) to eliminate the excitation laser beam. Following this process, the signals were recorded utilizing an s-CMOS camera (pco.edge 4.2, PCO AG) in the de-scanned frame. For fast imaging, PMT (H13543-20, Hamamatsu) was instrumented to efficiently identify and localize fluorescence targets and fluorophores.

For one-photon fluorescence point-scanning setup (see also Supplementary Fig. 10), a continuous-wave 488 nm monochromatic diode laser (OBIS 488-60 LS, Coherent) was employed as the excitation source. To mitigate interference from the excitation laser beam, a long-pass dichroic mirror (ZT488/640rpc-UF1, Chroma) and a long-pass filter (FELH0500, Thorlabs) were employed. The resulting signals were then captured using an s-CMOS camera (CS2100M-USB, Thorlabs). As discussed in the main text, the total acquisition time varies based on the severity of the scattering medium. It ranges from 52 to 260 seconds for a ROI measuring of  $30 \times 30 \mu\text{m}^2$ , with exposure times per sampling point ranging from 1 to 5 milliseconds.

### **Mouse brain preparation**

In the mouse brain imaging study, 12 weeks Thy1-EGFP lime M mice (Jackson Labs #007788) were anesthetized with an intraperitoneal injection of ketamine and xylazine before decapitation. Following the procedure, the cerebral organs were promptly extracted and placed in a refrigerated artificial cerebrospinal fluid (ACSF) environment. The entire brain was then sliced into 500  $\mu\text{m}$ -thick coronal sections and subjected to immunolabeling after an overnight fixation in paraformaldehyde at 4°C. The entire experimental process was carried out with the approval of the Committee of Animal Research Policy at Korea University (approval number: KUIACUC-2022-0013).

### **Acknowledgments**

This work was supported by the Institute for Basic Science (IBS-R023-D1). National Research Foundation of Korea (NRF) Grant Funded by the Korean Government (MSIT) (RS-2023-00213310).

## References

1. Gustafsson MGL. Surpassing the lateral resolution limit by a factor of two using structured illumination microscopy. *Journal of Microscopy*. 2000;198:82-87.
2. Muller CB, Enderlein J. Image scanning microscopy. *Phys Rev Lett*. 2010;104(19):198101.
3. Hell SW, Wichmann J. Breaking the Diffraction Resolution Limit by Stimulated-Emission - Stimulated-Emission-Depletion Fluorescence Microscopy. *Optics Letters*. 1994;19(11):780-782.
4. Betzig E, Patterson GH, Sougrat R, Lindwasser OW, Olenych S, Bonifacino JS, Davidson MW, Lippincott-Schwartz J, Hess HF. Imaging intracellular fluorescent proteins at nanometer resolution. *Science*. 2006;313(5793):1642-1645.
5. Hess ST, Girirajan TPK, Mason MD. Ultra-high resolution imaging by fluorescence photoactivation localization microscopy. *Biophysical Journal*. 2006;91(11):4258-4272.
6. Dertinger T, Colyer R, Iyer G, Weiss S, Enderlein J. Fast, background-free, 3D super-resolution optical fluctuation imaging (SOFI). *Proceedings of the National Academy of Sciences of the United States of America*. 2009;106(52):22287-22292.
7. Ji N. Adaptive optical fluorescence microscopy. *Nature Methods*. 2017;14(4):374-380.
8. Samanta K, Joseph J. An overview of structured illumination microscopy: recent advances and perspectives. *Journal of Optics*. 2021;23(12).
9. Rodríguez C, Ji N. Adaptive optical microscopy for neurobiology. *Current Opinion in Neurobiology*. 2018;50:83-91.
10. Wang K, Sun WZ, Richie CT, Harvey BK, Betzig E, Ji N. Direct wavefront sensing for high-resolution imaging in scattering tissue. *Nature Communications*. 2015;6.
11. Rodríguez C, Chen A, Rivera JA, Mohr MA, Liang YJ, Natan RG, Sun WZ, Milkie DE, Bifano TG, Chen XK, Ji N. An adaptive optics module for deep tissue multiphoton imaging in vivo. *Nature Methods*. 2021;18(10):1259-+.
12. Yoon S, Lee H, Hong JH, Lim YS, Choi W. Laser scanning reflection-matrix microscopy for aberration-free imaging through intact mouse skull. *Nature Communications*. 2020;11(1).
13. Hu Q, Hailstone M, Wang JY, Wincott M, Stoychev D, Atilgan H, Gala D, Chaiamarit T, Parton RM, Antonello J, Packer AM, Davis I, Booth MJ. Universal adaptive optics for microscopy through embedded neural network control. *Light-Science & Applications*. 2023;12(1).
14. Zheng W, Wu YC, Winter P, Fischer R, Nogare DD, Hong A, McCormick C, Christensen R, Dempsey WP, Arnold DB, Zimmerberg J, Chitnis A, Sellers J, Waterman C, Shroff H. Adaptive optics improves multiphoton super-resolution imaging. *Nature Methods*. 2017;14(9):869-+.
15. Lin RZ, Kipreos ET, Zhu J, Khang CH, Kner P. Subcellular three-dimensional imaging deep through multicellular thick samples by structured illumination microscopy and adaptive optics. *Nature Communications*. 2021;12(1).
16. Thomas B, Wolstenholme A, Chaudhari SN, Kipreos ET, Kner P. Enhanced resolution through thick tissue with structured illumination and adaptive optics. *Journal of Biomedical Optics*. 2015;20(2).
17. Paidi SK, Zhang QR, Yang YH, Xia CH, Ji N, Gong XH. Adaptive Optical Two-Photon Fluorescence Microscopy Probes Cellular Organization of Ocular Lenses In Vivo. *Investigative Ophthalmology & Visual Science*. 2023;64(7).
18. Sage D, Donati L, Soulez F, Fortun D, Schmit G, Seitz A, Guet R, Vonesch C, Unser M. DeconvolutionLab2: An open-source software for deconvolution microscopy. *Methods*. 2017;115:28-41.
19. Rai MR, Rosen J. Optical incoherent synthetic aperture imaging by superposition of phase-shifted optical transfer functions. *Optics Letters*. 2021;46(7):1712-1715.
20. Xiang M, Pan A, Zhao YY, Fan XW, Zhao H, Li C, Yao BL. Coherent synthetic aperture imaging for visible remote sensing via reflective Fourier ptychography. *Optics Letters*. 2021;46(1):29-32.
21. Kang S, Jeong S, Choi W, Ko H, Yang TD, Joo JH, Lee JS, Lim YS, Park QH, Choi W. Imaging deep within a scattering medium using collective accumulation of single-scattered waves. *Nature Photonics*. 2015;9(4):253-258.
22. Debarre D, Booth MJ, Wilson T. Image based adaptive optics through optimisation of low spatial frequencies. *Optics Express*. 2007;15(13):8176-8190.
23. Pu D, Pan XC, Tao H, Liu C, Zhu JQ. Iterative reconstruction method for the accurate measurement of optical transfer function. *Applied Optics*. 2021;60(26):8164-8173.
24. Zunino A, Castello M, Vicidomini G. Reconstructing the image scanning microscopy dataset: an inverse problem. *Inverse Problems*. 2023;39(6).
25. Yoon K, Han KY, Tadesse K, Mandracchia B, Jia S. Simultaneous Multicolor Multifocal

Scanning Microscopy. *Acs Photonics*. 2023;10(9):3035-3041.

26. York AG, Parekh SH, Nogare DD, Fischer RS, Temprine K, Mione M, Chitnis AB, Combs CA, Shroff H. Resolution doubling in live, multicellular organisms via multifocal structured illumination microscopy. *Nature Methods*. 2012;9(7):749-U167.

27. Chen W, Natan RG, Yang YH, Chou SW, Zhang QR, Isacoff EY, Ji N. In vivo volumetric imaging of calcium and glutamate activity at synapses with high spatiotemporal resolution. *Nature Communications*. 2021;12(1).

28. Li SW, Wu JJ, Li H, Lin DY, Yu B, Qu JL. Rapid 3D image scanning microscopy with multi-spot excitation and double-helix point spread function detection. *Optics Express*. 2018;26(18):23585-23593.

29. Wu JL, Ji N, Tsia KK. Speed scaling in multiphoton fluorescence microscopy. *Nature Photonics*. 2021;15(11):800-812.

30. Zhang CS, Yu B, Lin FR, Samanta S, Yu HH, Zhang W, Jing YY, Shang CF, Lin DY, Si K, Gong W, Qu JL. Deep tissue super-resolution imaging with adaptive optical two-photon multifocal structured illumination microscopy. *Photonix*. 2023;4(1).

31. Zheng JJ, Fang X, Wen K, Li JY, Ma Y, Liu M, An S, Li JL, Zalevsky Z, Gao P. Large-field lattice structured illumination microscopy. *Optics Express*. 2022;30(15):27951-27966.

32. Koho SV, Slenders E, Tortarolo G, Castello M, Buttafava M, Villa F, Tcarenkova E, Ameloot M, Bianchini P, Sheppard CJR, Diaspro A, Tosi A, Vicidomini G. Two-photon image-scanning microscopy with SPAD array and blind image reconstruction. *Biomedical Optics Express*. 2020;11(6):2905-2924.

33. Park S, Jo Y, Kang M, Hong JH, Ko S, Kim S, Park S, Park HC, Shim SH, Choi W. Label-free adaptive optics single-molecule localization microscopy for whole zebrafish. *Nature Communications*. 2023;14(1).